



Surface modification of collagen using low-energy noble gas ion implantation

Jérôme Leveueur^{a,b}, Yi Zhang^{b,c}, Holger Fiedler^{a,*}, Sujay Prabakar^c, Eric C. Le Ru^b, John Kennedy^{a,b}

^a GNS Science, National Isotope Centre, Lower Hutt, New Zealand

^b The MacDiarmid Institute for Advanced Materials and Nanotechnology, School of Chemical and Physical Sciences, Victoria University of Wellington, Wellington, New Zealand

^c Leather and Shoe Research Association of New Zealand, Palmerston North, New Zealand

ARTICLE INFO

Keywords:

Collagen
Ion implantation
Noble gases
Raman spectroscopy
FTIR spectroscopy
Monte-Carlo simulation

ABSTRACT

Due to its versatility, biodegradability, and biocompatibility, collagen is an increasingly important building block for sustainable manufacturing. Consequently, it is becoming more important to develop methods to tune collagen's properties for a given application. We propose employing a tool often reserved to microelectronics, low-energy ion implantation, to modify the top surface of collagen sheets, increasing surface sp^2 carbon without altering significantly the amide structure while retaining the bulk properties of collagen. Implantation of He^+ , Ne^+ , Ar^+ and Xe^+ was performed at varying energies from 5 to 25 keV, with beam current density from 5×10^{-2} to $5 \mu A cm^{-2}$. The resulting changes in chemical structure were investigated using Raman and FTIR spectroscopies. Monte Carlo simulations of the interaction of the ion beams with collagen are used to quantify the energy deposited in the implanted module. A model is proposed that relates the observed changes to these ion implantation conditions.

1. Introduction

Collagen is an abundant protein found in meat processing byproducts such as skin, tendon, and bone [1]. The use of collagen and collagen-derived products has been growing steadily over the past 50 years [1–4]. The primary applications of collagen are food and cosmetics [5], while nowadays it is increasingly used in making high-value advanced materials [6]. Its biocompatibility and weak antigenicity compared to synthetic polymers make it a prime candidate in biomedical applications [7,8]. Also, its biodegradability and polymeric nature allow transformative applications as eco-friendly packaging materials [9]. Consequently, there is a continuous interest in collagen processing technologies especially on surface characteristics to further increase its usability and interoperability beyond traditional applications, as well as to develop collagen-based electronics and biocompostable materials [3,10–16]. For instance, variations in the surface roughness of the biomaterials can induce differences in cell responses: epithelial and periodontal fibroblast cells tend to attach to smooth surfaces, while osteoblast cells prefer rough surfaces [16]. The surface properties can

also determine the surface free energy and the wettability of collagen composite films to improve their applications as packaging materials [5,17,18].

There are multiple methods to chemically and physically modify the surface characteristics of collagen materials. Although chemical methods provide promising controllability and uniformity, physical methods in general have advantages in safety, cost-effectiveness and biocompatibility [16,19]. Physical treatments have been used extensively in biomaterial processing, with methods including dehydrothermal treatment (DHT), UV, γ , β irradiations, and ion implantations [1,20–23]. While dehydration of collagen materials enhances physical interactions between collagen molecules, irradiation and ion implantation can influence surface chemistry and cell attachment properties [1,16,20].

Ion implantation is a well-established technique to modify precisely the surface properties of the materials. Bombarding a material's surface with energetic ions can induce changes in the elemental composition as well as short and long-range ordering in the materials [24]. Sputtering from ion interactions can also be used for smoothing, increasing

* Corresponding author.

E-mail address: h.fiedler@gns.cri.nz (H. Fiedler).

<https://doi.org/10.1016/j.surfcoat.2023.129768>

Received 20 April 2023; Received in revised form 29 May 2023; Accepted 28 June 2023

Available online 29 June 2023

0257-8972/© 2023 Elsevier B.V. All rights reserved.

Table 1

Ion implantation conditions. Experimental parameter variabilities include acceleration voltage ± 0.1 kV, current density ± 5 %, and fluence $\pm 10^{13}$ cm $^{-2}$.

#	Implanted species	Ion energy (keV)	Current density ($\mu\text{A cm}^{-2}$)	Fluence (cm $^{-2}$)
1	NA (Control)	0	0	0
2	Ar	5	0.1	5×10^{14}
3	Ar	10	0.1	5×10^{14}
4	Ar	20	0.1	5×10^{14}
5	Ar	25	0.1	5×10^{14}
6	Ar	15	0.05	5×10^{14}
7	Ar	15	0.1	5×10^{14}
8	Ar	15	0.2	5×10^{14}
9	Ar	15	0.5	5×10^{14}
10	Ar	15	1	5×10^{14}
11	Ar	15	2	5×10^{14}
12	Ar	15	5	5×10^{14}
13	Ar	15	0.1	1×10^{12}
14	Ar	15	0.1	1×10^{13}
15	Ar	15	0.1	1×10^{14}
16	Ar	15	0.1	2×10^{14}
17	Ar	15	0.1	1×10^{15}
18	Ar	15	0.1	5×10^{15}
19	Ar	15	0.1	1×10^{16}
20	Ar	15	5	5×10^{15}
21	Ar	15	5	1×10^{16}
22	Ar	15	5	5×10^{16}
23	Ar	15	5	1×10^{17}
24	Ar	15	5	2×10^{17}
25	He	15	0.1	5×10^{14}
26	He	15	0.1	1×10^{15}
27	He	15	0.1	5×10^{15}
28	Ne	15	0.1	5×10^{14}
29	Ne	15	0.1	1×10^{15}
30	Ne	15	0.1	5×10^{15}
31	Xe	15	0.1	5×10^{14}
32	Xe	15	0.1	1×10^{15}
33	Xe	15	0.1	5×10^{15}

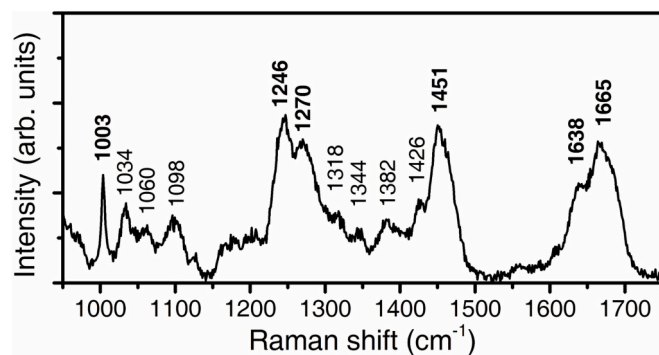


Fig. 1. Raman spectrum of pristine control collagen sheet, highlighting the characteristic peaks.

roughness, and even patterning surfaces [25,26]. As a result, the ion implantation technique has been used extensively to control the electronic properties and morphology of semiconductor materials [24,27,28]. Beyond the microelectronics industry, however, industrial uptake of ion implantation has been limited. This is now changing as new systems are being developed that enable the use of ion implantation at a large scale [29–31], which would benefit materials and applications that were previously considered beyond the scope of this technique.

A key advantage of ion implantation on organic materials is that it allows drastic surface modifications of the molecular structure (with ~ 5 nm depth precision) without affecting the bulk of the material [27]. The mechanism behind ion beam surface modification starts from the formation of radicals during bond breakage, resulting in chain shortening in polymeric molecules and the formation of new chemical bonds and associated improved functionality [32–36]. This effect has been

Table 2

Assignment of peaks in the Raman spectra of control collagen sheets and emerging peaks found in the Raman spectra after Ar $^{+}$ ion beam implantation.

Control (cm $^{-1}$)	Ar (cm $^{-1}$)	Assignment	References (cm $^{-1}$)
	1679	Amide I, β -sheet	1670–1675 [48,49,52]
1665		Amide I, α -helix	1655–1670 [48,52,54]
1638sh		Amide I, 3_{10} -helix	1632–1642 [48,49,54]
	1591br	G mode (E_{2g}), in-plane ν (C–C, sp^2)	1580 [56,57]
1451		δ (CH $_2$); δ (CH $_3$)	1445–1457 [49,50]
1426sh		ν_s (COO $^-$); δ (C–OH)	1410–1425 [48,54,58,59]
1382w		ν_s (COO $^-$)	1380–1392 [49,50,54,60,61]
1344w		ω (CH $_2$); ω (CH $_3$)	1340–1343 [48,50,54,62]
1318w		τ (CH $_2$); τ (CH $_3$)	1314–1318 [48,50,54,62]
	1310br	D breathing mode (A_{1g}), in-plane ν (C–C, sp^2)	1310–1330 [57]
1270		Amide III, α -helix	1265–1271 [48,51,52]
1246		Amide III, random coil	1235–1248 [48,51,52]
1098		ν_{as} (COC)	1094–1100 [54,55]
1060		ν_{18b} , Phe a	1062–1065 [49,54]
1034		ν (C–C), Pro; ν_{18a} , Phe	1031–1037 [48,49,54]
1003		ν (C–C), ν_{12} , Phe	995–1006 [49,50,54]

Notations (same for FT-IR): ν , stretching (s = symmetrical, as = asymmetrical); δ , bending; ω , wagging; τ , twisting; sh, shoulder; br, broad; w, weak;

^a : Wilson notation for modes of benzene ring vibration [[63]].

exploited to modify the surface of biomaterials by plasma immersion ion implantation (PIII) [22,23,37]. PIII relies on a pulsed high voltage bias to form a reactive ions which are subsequently accelerated onto the target [38]. In contrast to classic ion implantation, the absence of beam focusing equipment reduces cost but also causes large variation of the implantation energy at the substrate and the angle of implantation. Hence, for PIII the separation of chemical modification and ballistic collision cascades is extremely complex. One of the few previous investigations on ion irradiations with a fixed energy of the collagen coating layer showed improvements in cell adhesion [20]. However, high-energy ion implantation (> 100 keV) was used, which leads to much deeper ion penetration which reduces significantly the degree and types of chemical changes occurring on the surface. In this case, interactions within the first 0 to 30 nm are dominated by electronic energy loss instead of nuclear energy loss [27], yielding modifications similar to UV exposure [35]. Because of their focus on high energy (> 100 keV), even the higher fluence in previous ion beam modification of collagen studies are expected to have a low number of changes per incident atoms compared to the implantation conditions in our investigation. Only at very high fluences (5×10^{17} cm $^{-2}$), are previous studies reaching similar levels of deposited energy per unit volume. Furthermore, it is difficult to readily separate effects on collagen that are due to direct ballistic modifications or through heating the collagen. Typically, the power density used in previous investigations with $0.5 \mu\text{A cm}^{-2}$ and 150 keV already are bringing a power density as high as the highest power density in this investigation (75 mW cm^{-2}) [39].

Herein, our investigation focuses on low-energy ion implantation (< 100 keV), which primarily induces changes at the surface and modifications dominated by nuclear energy loss; similar to the energy expected in PIII studies [22]. To our knowledge, this work provides the first systematic investigation of key implantation parameters for noble gas implantation into collagen at low energy, which would potentially expand the application of the technique as well as provide a way to modify the structure and chemistry in collagenous materials for biomedical applications through a physical method. A range of implantation fluence, beam energy (5–25 keV) and ion beam (0.05 – $5 \mu\text{A cm}^{-2}$) current density was investigated using He $^{+}$, Ne $^{+}$, Ar $^{+}$ and Xe $^{+}$ beams. Analyses using Raman spectroscopy and Fourier transform

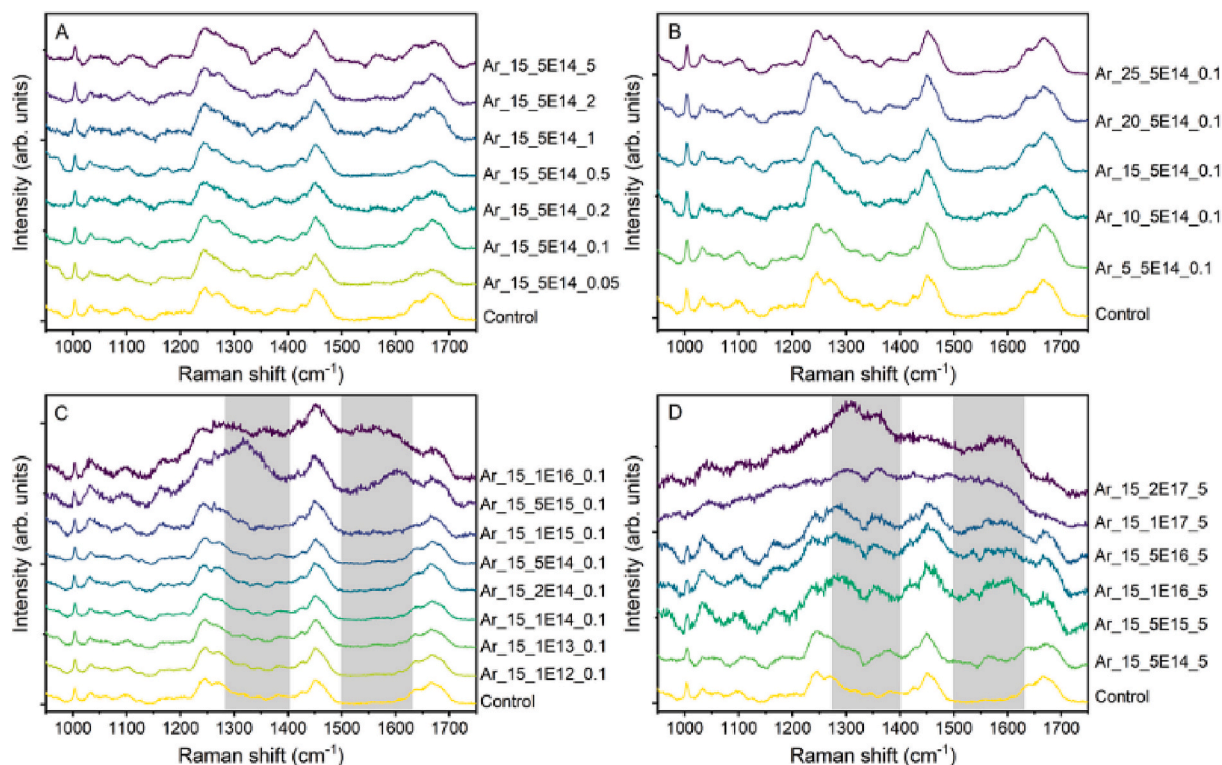


Fig. 2. Stacked Raman spectra of collagen sheets implanted by Ar^+ ion at different conditions. Samples are named “Implanted Element_Energy (KeV)_Fluence (cm^{-2})_Current Density ($\mu\text{A cm}^{-2}$)”, same as below. Grey shadings in C and D are placed to highlight the peaks of carbonaceous species.

infrared spectroscopy (FT-IR) combined with Monte Carlo simulations of the interactions of the ion beams with collagen provide insights into the types of changes occurring in the implanted range. A model is proposed to relate the observed changes to these ion implantation conditions.

2. Experimental section

2.1. Materials

Collagen was extracted from bovine limed splits according to an established procedure [40,41], with some modifications. In brief, frozen lime split samples were delimed with 2 % NH_4Cl and 0.5 % HCl for 60 min at 4 °C. Delimed pieces were rinsed with distilled water before suspending in 10 volumes of prechilled 0.5 M acetic acid containing 1.0 wt% pepsin (2336 FIP-U/mg, BIP1008, Apollo Scientific, Stockport, United Kingdom). Collagen was extracted at 4 °C with constant stirring for 24 h. Collagen supernatant was collected via centrifugation at $15,317 \times g$ for 30 min to remove insoluble protein. Collagen was salted out using a final concentration of 2.0 M NaCl , the resulting precipitate was collected by centrifugation, dissolved in 0.5 M acetic acid and dialysed against 0.05 M acetic acid at 4 °C for 3 days. Resulting solution was freeze-dried and stored. Prior ion implantation experiments collagen sheet were cut into sizes of 15 mm \times 15 mm \times 2 mm (L \times W \times H).

2.2. Ion beam surface modification

Ion implantation experiments were performed using the GNS Science Medium Energy Ion Implanter which allows implantation on 1 cm^2 samples [42,43]. The base pressure was kept at 5×10^{-7} mbar, with operating pressure at $<10^{-6}$ mbar. Single charge implanted species were produced from the various noble gases He, Ne, Ar, and Xe (>99 % purity) with a Penning gas ion source. Acceleration voltages ranging from 5 kV to 25 kV were used. A double focusing electromagnet is used to

select the mass of the element. The dependence on the current density of the ion beam was investigated by varying the ion beam current between 0.05 μA and 5 μA over an electrostatically-scanned surface area of 1 cm^2 . The collagen surface is located perpendicular to the ion beam. The initial temperature was between 20 °C and 22 °C. As the collagen samples were poor conductors and to reduce charge build-up, the samples were mounted on the sample holder using carbon tape. After ion implantation, the samples were kept in individual plastic bags before characterisation. Detailed treatment conditions are listed in Table 1.

2.3. Chemical characterisation

Raman spectroscopy and FT-IR spectroscopy were performed on each sample to resolve changes in the collagen chemical structure.

Raman spectra were collected using a LabRam HR spectrometer (Horiba Jobin-Yvon) equipped with a Symphony CCD detector cooled at -130 °C using liquid N_2 , in a backscattering configuration through an Olympus SLM Plan N 100 \times /NA0.60 air objective by focusing on the air/solid interface. Collagen samples were excited using 633 nm at approximately 10 mW, for an exposure time of 20 s with 10 accumulations. The spectra were corrected to remove the fluorescence of collagen through polynomial fittings. The peak ratios are calculated from the corrected intensities at the peak centres.

FT-IR measurements were carried out using iD5 ATR on Nicolet™ iS5 Spectrometer (ThermoFisher Scientific) in an attenuated total reflectance (ATR) mode with a zinc selenide (ZnSe) crystal. Collagen samples were loaded and measured at a frequency interval of from 600 cm^{-1} to 4000 cm^{-1} . The number of scanning and resolution was set at 16 and 4 cm^{-1} , respectively.

2.4. Monte Carlo simulations of ion implantations

Monte Carlo simulations were undertaken using the SDTRIMSP software package [44]. This programme simulates individual

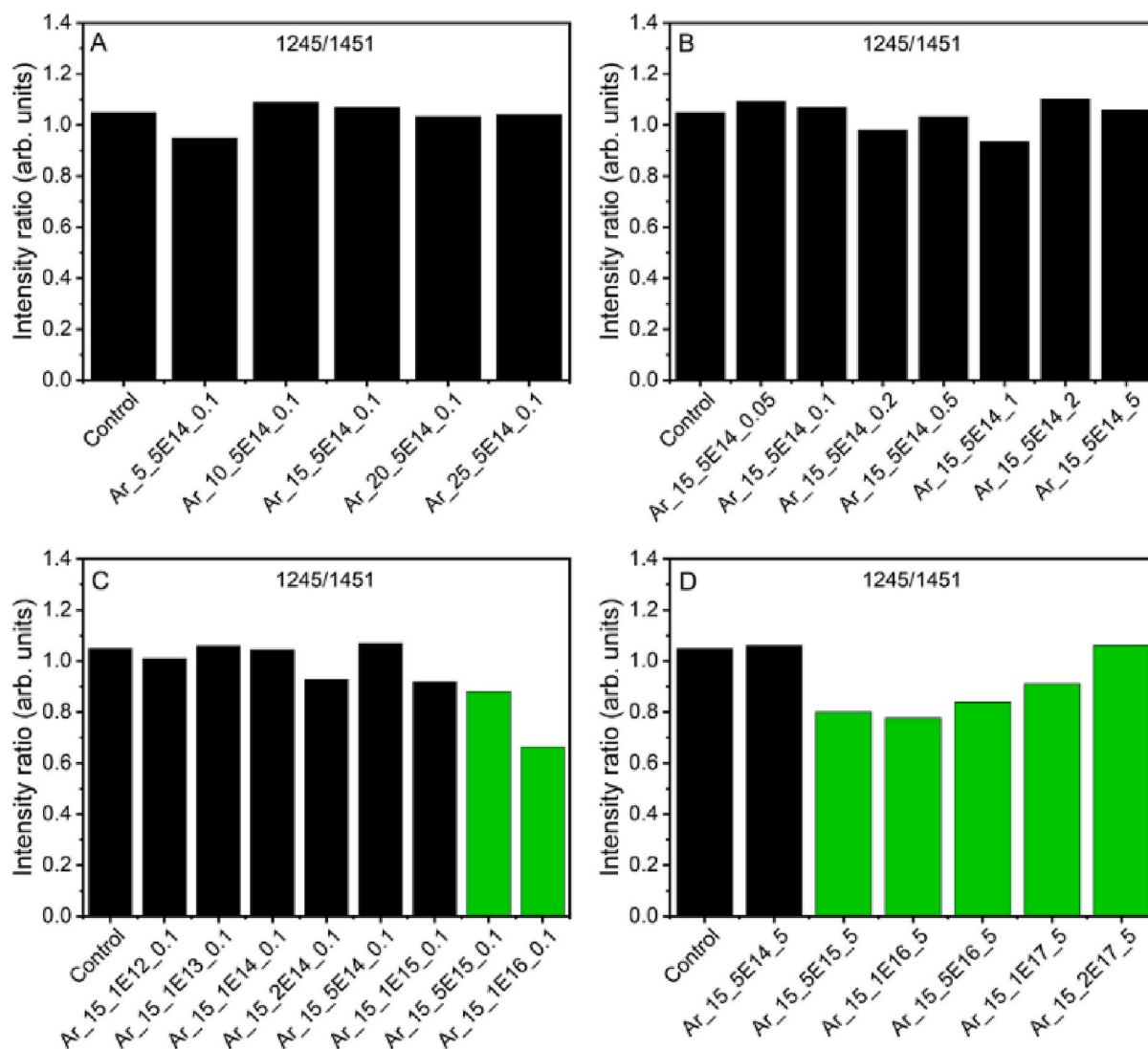


Fig. 3. Ratios of the intensity of 1245 cm^{-1} and 1451 cm^{-1} peaks in the Raman spectra of collagen sheets implanted by Ar^+ ions at different conditions. Green colouring highlights the results from spectra with significant carbonaceous features.

implantation cascade and accounts for changes in the implanted target composition during the implantation. SDTrimSP solely calculates nuclear and electronic interactions, while chemical reactions are not considered. Further, the theory is based on amorphous material which limits its applicability to crystalline materials. Nonetheless, simulation provides valuable insight into the effects of noble gas ion implantation and the emerging recoil cascade.

For the presented simulations we assume that once displaced atoms will not rebind to collagen. Collagen was simulated with the stoichiometry $\text{C}_{12}\text{N}_3\text{O}_4\text{H}_{17}$ and a density of 1.3 g cm^{-3} . For the surface binding energies (SBE) and displacement energies (DE), the following values were used in the simulations: Carbon (SBE: 3.5 eV; DE: 15 eV), oxygen (SBE: 2.58 eV; DE: 5 eV), nitrogen (SBE: 4.9 eV; DE: 25 eV) and hydrogen (SBE: 1.1 eV; DE: 5 eV).

A detailed approach to simulating the thermal effects was described previously [45]. The input beam power densities were calculated from the beam energy and current density. The chosen thickness of the volume heated during the implantation was that of an individual collagen layer. This is justified by the layered and porous nature of the samples and the poor heat conductivity of collagen ($5.3 \times 10^{-1}\text{ W m}^{-1}\text{ K}^{-1}$) [46]. The heat capacity (in $\text{J g}^{-1}\text{ K}^{-1}$) of dry collagen was approximated as the linear function $C_p(T) = aT - b$, with $a = 3.34 \pm 1.38 \times 10^{-2}\text{ J g}^{-1}\text{ K}^{-2}$ and $b = 4.48 \pm 0.07 \times 10^{-3}\text{ J g}^{-1}\text{ K}^{-1}$. This linear fit ($R^2 = 0.99559$) is

retrieved from experimental heat capacity data measured by adiabatic calorimetry obtained from Pyda et al. [47] Equilibrium is reached after about 2 s, which is equivalent to an implanted fluence of $6.3 \times 10^{13}\text{ cm}^{-2}$.

3. Results and discussion

Visual observation of the implanted collagen showed a slight discolouration after ion implantation. To determine the extent of the change on the surface of the samples, we characterised the chemical structure of collagen by Raman and FT-IR spectroscopy.

3.1. Raman Spectroscopy

A typical Raman spectrum of dry collagen is observed in the pristine control (Fig. 1), showing the main characteristic peaks including amide I from the stretching of the $\text{C}=\text{O}$ bond in combination with deformation of the $\text{N}-\text{H}$ bond (1665 cm^{-1} and 1638 cm^{-1}), $\text{C}-\text{H}$ bending (1451 cm^{-1}), amide III from the stretching of $\text{C}-\text{N}$ bond and the deformation of $\text{N}-\text{H}$ bond (1270 and 1246 cm^{-1}), and the benzene ring breathing mode of $\text{C}-\text{C}$ bonds in phenylalanine (Phe) (1003 cm^{-1}) [48–55]. Detailed assignments are listed in Table 2.

When implanted by Ar^+ ions, the spectrum of collagen undergoes a

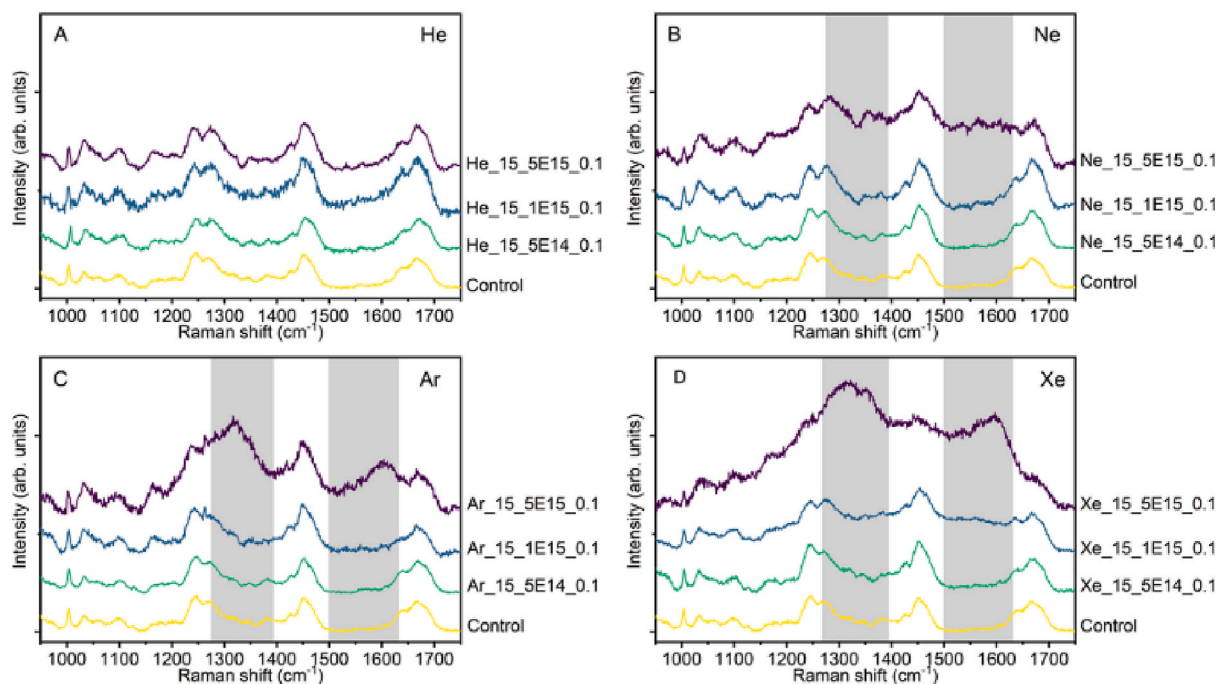


Fig. 4. Stacked Raman spectra of collagen sheets implanted by He⁺, Ne⁺ and Xe⁺ ions compared to Ar⁺ ion at different conditions. Grey shadings in B, C and D are placed to highlight the peaks of carbonaceous species.

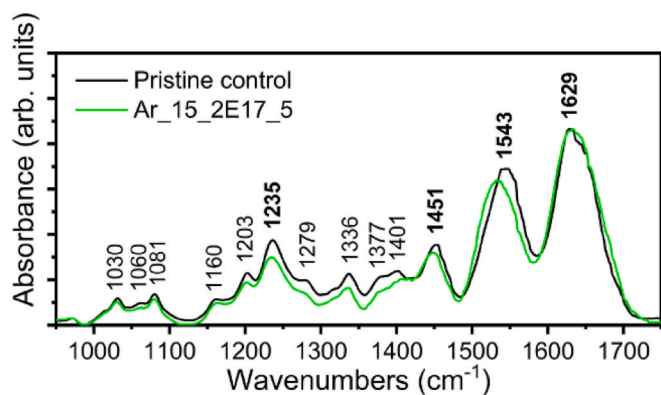


Fig. 5. FT-IR spectrum of pristine control collagen sheet (black) and Ar_{15_2E17_5} (green), highlighting the major assignable peaks.

Table 3
Assignment of FT-IR peaks in the spectra of the native collagen sheets.

Raman shift (cm ⁻¹)	Assignment	Reference (cm ⁻¹)
1629	Amide I, ν(C=O)	1600–1700, 1650 [68,69,72]
1543	Amide II, δ(N–H) and ν(C–N)	1500–1600, 1550 [68,72]
1451	δ(CH ₂); δ(CH ₃)	1450 [69,72]
1401	ν _s (COO ⁻)	1400–1410 [72,73]
1377sh	δ(CH ₃), glycosaminoglycans (GAGs)	1376 [72]
1336	ω(CH ₂), Pro	1337 [70]
1279sh	Amide III, δ(N–H); ω(CH ₂), Gly backbone or Pro	1280 [68–71]
1235	Amide III, ν(C–N)	1240 [68–71]
1203	Amide III	1204 [71]
1160	ν(C–O), carbohydrate residues	1160 [72]
1081	ν(C–O), carbohydrate residues	1080 [72]
1060	ν(C–O), carbohydrate residues	1064 [72]
1030	ν(C–O), carbohydrate residues	1032 [72]

series of changes (Fig. 2). The beam energy, fluence, and current density are individually adjusted to study the effect on the secondary structure of collagen. We observed minor fluctuations in peak intensities at low beam energy, fluence, and current densities, whereas at high fluences significant disruptions and emerging broad peaks were identified.

In the literature, the intensity ratios of 1665 cm⁻¹ to 1638 cm⁻¹ peaks and 1245 cm⁻¹ to 1270 cm⁻¹ peaks were used to indicate the translation from triple helical to disordered structures in the collagen molecules [53,64]. However, it was also reported that the intensity of 1665 cm⁻¹, 1638 cm⁻¹ and 1270 cm⁻¹ peaks are highly sensitive to the relative orientation of the collagen fibres to the incident laser, whereas 1245 cm⁻¹ and 1451 cm⁻¹ peaks are largely isotropic [53,65–67]. Therefore, the use of intensity ratio 1665/1638 or 1245/1270 as indicators for collagen structural changes can be limited to isotropic collagen substrates. In this study, we observed intensity fluctuations in 1665 cm⁻¹, 1638 cm⁻¹ and 1270 cm⁻¹ peaks, showing anisotropic fibre orientations in the collagen sheets, while 1245 cm⁻¹ and 1451 cm⁻¹ peaks remained unaffected (Fig. 2A).

If collagen denatures by the localised thermal effects during ion implantation, it would undergo conformational changes indicated by an increase in the peak intensity at 1245 cm⁻¹ (amide III, random coil). If collagen degrades by breakages at the amide bonds, we expect to see a decrease in the peak intensity at 1245 cm⁻¹. If the bond breakage occurs in the aliphatic –CH₂– or –CH₃ groups in collagen backbone or side chains, we would observe a decrease in the peak intensity at 1451 cm⁻¹. Hence, considering the pair of 1245 cm⁻¹ and 1451 cm⁻¹, one may derive a more reliable indicator based on the 1245/1451 ratio for the changes in the conformational structure of collagen and the C–H bonds by ion beam implantation.

When the Ar⁺ fluence was below 10¹⁵ cm⁻², the 1245/1451 ratio remained largely unchanged irrespective of the variations in ion energy and ion beam current (Fig. 3A, B, C and D). At higher fluences, we observed a decrease in the 1245/1451 ratio followed by a gradual increase at fluences above 10¹⁶ cm⁻² (Fig. 3C and D). The decreases in the ratio indicate the breakage of amide bonds, and the increases at high fluences show the bond breakage at aliphatic –CH₂– or –CH₃ groups. The latter was confirmed by the emerging broad peaks at 1310 cm⁻¹ and

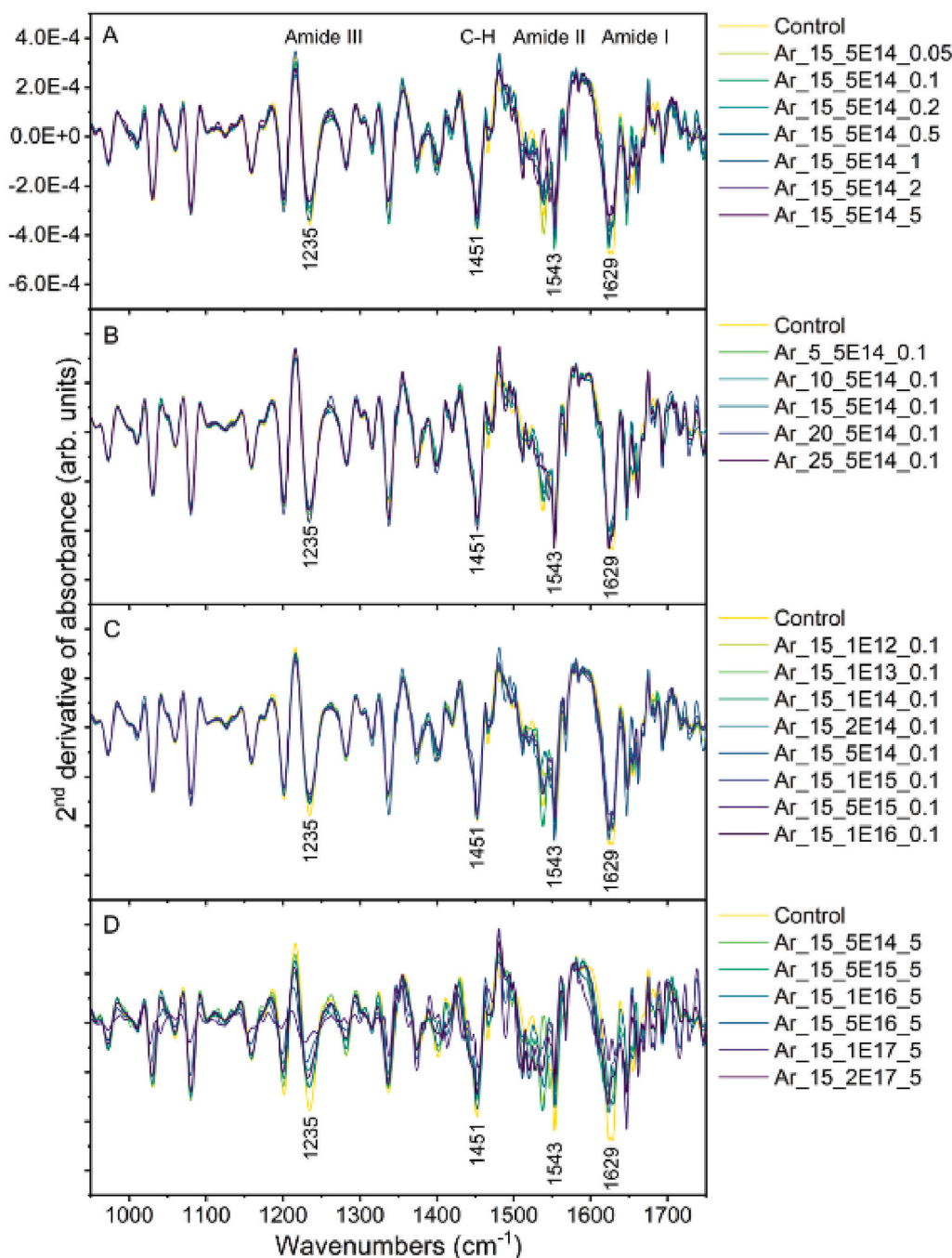


Fig. 6. The second derivative of the absorbance in FT-IR spectra of collagen sheets implanted with Ar^+ ion at different conditions. The same scale is applied to all y-axes.

1591 cm^{-1} (Fig. 3D and Table 2) highlighting the carbonisation of collagen surface via the conversion of sp^3 carbon (e.g., $-\text{CH}_2-$ or $-\text{CH}_3$ groups) into sp^2 carbon ($\text{C}=\text{C}$ bonds) at high fluences [56].

Furthermore, we have investigated the effect of ion species using He, Ne, or Xe in replacement of Ar, at an energy of 15 keV and a current density of $0.1\ \mu\text{A cm}^{-2}$, within a narrower range of fluence from 5×10^{14} to $5 \times 10^{15}\text{ cm}^{-2}$. As shown in Fig. 4, He^+ led to the least carbonisation, while Xe^+ resulted in the highest level of carbonisation indicated by the strong broad amorphous sp^2 carbon peaks.

3.2. Fourier transform infrared spectroscopy (FT-IR)

FT-IR was also used to investigate the structural changes in collagen

upon ion implantation to support the information acquired from Raman spectroscopy. Fig. 5 showed a characteristic IR absorption spectrum of native collagen. The typical peaks are assigned to amide I (1629 cm^{-1}), amide II (1543 cm^{-1}), C–H bending (1451 cm^{-1}) and amide III (1235 cm^{-1}) [68–73]. Detailed assignments are listed in Table 3. When the collagen sheets were implanted using the ion beams, only minor changes were observed in the FT-IR spectra, giving the most significant intensity changes in the amide II and amide III peaks.

To highlight the minor changes in the FT-IR spectra induced by ion implantation, we calculated the second derivative of the infrared absorbance and stacked it over the native collagen spectrum (Fig. 6) [72]. Only minor changes in the conformation of peptide backbones were found at low fluence (Fig. 6A, B and C), agreeing with the Raman

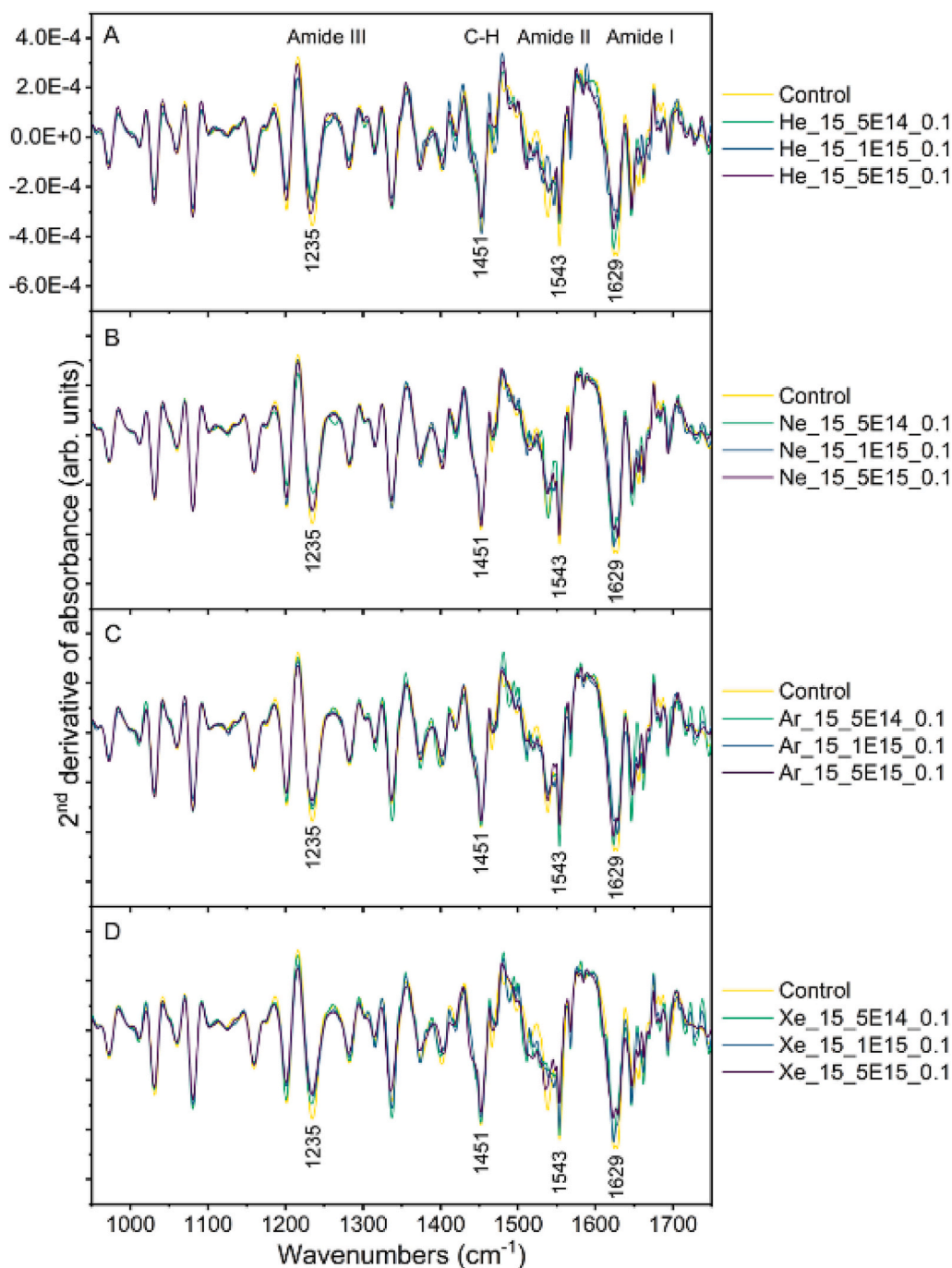


Fig. 7. The second derivative of the absorbance in FT-IR spectra of collagen sheets implanted by He⁺, Ne⁺, and Xe⁺ ions compared to Ar⁺ ion at different conditions. The same scales are applied to all y-axes.

spectroscopy observations. The changes in backbone conformation mainly disturb the coupled vibrations of C–N stretching and N–H bending in the amide II mode, with a slight impact on the C=O stretching in the amide I mode. Lesser impacts were found in amide III mode with Ar⁺ ion implantation. However, when the fluence goes higher at a high current density (5 $\mu\text{A cm}^{-2}$), major disruption of the structure was observed (Fig. 6D). The amide peaks significantly diminished and the peak at 1451 cm^{-1} (C–H bending mode) also decreased. This observation coincides with the formation of carbonaceous species from the –CH₂– and –CH₃ groups in collagen. Similarly, the effects of ion implantation using different gaseous species (He, Ne, and Xe) are analysed based on the second derivative of IR absorbance (Fig. 7). Due to the low fluence in the study of different gases, we observed similar

minor changes in the amide regions in the IR spectra for all ion species.

3.3. Ion implantation simulations

To understand further the mechanisms involved in the different implantation conditions, we simulated the interactions of the ion beam with collagen and discussed the nuclear and electronic stopping power, thermal effects, and the impacts of the ion beams on the elemental composition of collagen.

Nuclear and electronic stopping power. Ions of different energy and mass have varying nuclear and electronic stopping power [24,27]. Fig. 8 summarises the nuclear and electronic stopping power for the different ion beams. With an increasing mass of the implanted noble gas, the

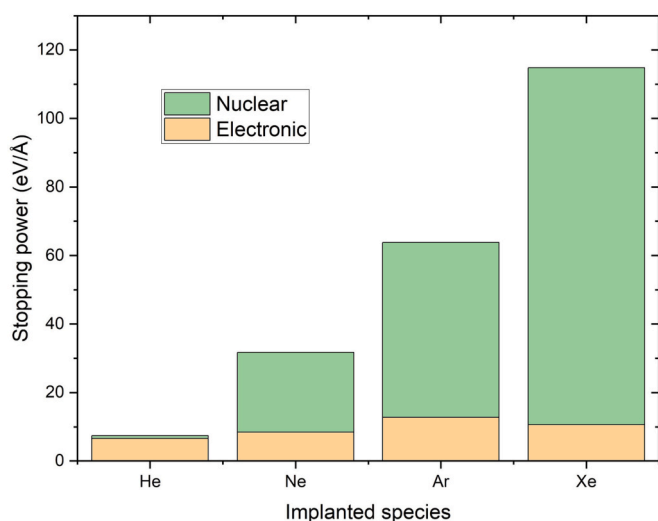


Fig. 8. Nuclear and electronic stopping power for the different implanted species.

nuclear stopping becomes more dominant, which causes more displacement of atoms on the collagen backbone, matching the stronger bond breakage and the subsequent carbonisation effects observed in Raman spectra of collagen treated by Xe and Ar compared to Ne and He (Fig. 4).

Thermal effects. The modification from the nuclear and electronic interactions, and doping if the implanted species is chemically active, occur only in the implantation range, which is often a lot smaller than the sample thickness. This is true provided that the power density of the ion beam doesn't lead to a significant increase in temperature over the bulk of the sample over the duration of the implantation. This can be difficult to control as the vacuum needed for the implantation can thermally insulate the sample, and radiative losses are the only cooling mechanism.

We simulated the thermal effects based on the experimental

parameters during the ion beam treatments, the estimations of heat capacity and geometry of the target, while assuming no conduction loss. The detailed approach has been described previously [45]. The different input beam power densities were calculated from the different beam energy and current density. The chosen thickness of the volume heated during the implantation was that of an individual collagen layer. This is justified by the layered and porous nature of the samples and the poor heat conductivity of collagen ($5.3 \times 10^{-1} \text{ W m}^{-1} \text{ K}^{-1}$) [46]. The heat capacity (in $\text{J g}^{-1} \text{ K}^{-1}$) of dry collagen was approximated as the linear function $C_p(T) = aT - b$, with $a = 3.34 \pm 1.38 \times 10^{-2} \text{ J g}^{-1} \text{ K}^{-2}$ and $b = 4.48 \pm 0.07 \times 10^{-3} \text{ J g}^{-1} \text{ K}^{-1}$.

This linear fit ($R^2 = 0.99559$) is retrieved from experimental heat capacity data measured by adiabatic calorimetry obtained from Pyda et al. [47] Doing so, the maximum temperature rise during any of the implantation was 85.4 K. Fig. 9 shows the calculated temperature profile at different ion energy and assumes the highest current density used in this investigation ($5 \mu\text{A cm}^{-2}$).

Equilibrium is reached after about 2 s. In this time an equivalent fluence of $6.3 \times 10^{13} \text{ cm}^{-2}$ is implanted. The temperature rise is markedly lower than the temperatures required to degrade collagen ($>495 \text{ K}$). Consequently, thermal effects are considered negligible for this set of experiments. As suggested in the introduction, the thermal budget of previous investigation studies is high enough to significantly increase the temperature of the sample beyond its denaturation temperature. Using the same calculation with $0.5 \mu\text{A cm}^{-2}$ and 150 keV the maximum increase in temperature at equilibrium is 293 K. Equilibrium is reached in about 0.25 s with a sample thickness of 100 μm and 2.4 s with a sample thickness of 1 mm. Methods to mount the samples will drastically affect the equilibrium temperature.

Ion beam modification profile. Ion beam implantation directly introduces ions to the material while also altering the elemental composition of the treated material. Here we simulated the interactions between the noble gas ions and collagen to provide a quantitative view of the implanted elements and the changes in the hydrogen/carbon (H/C) ratio of collagen on the surface.

A series of Ar implantation simulations were carried out at different fluences, showing an increase in the presence of Ar in the collagen sheet

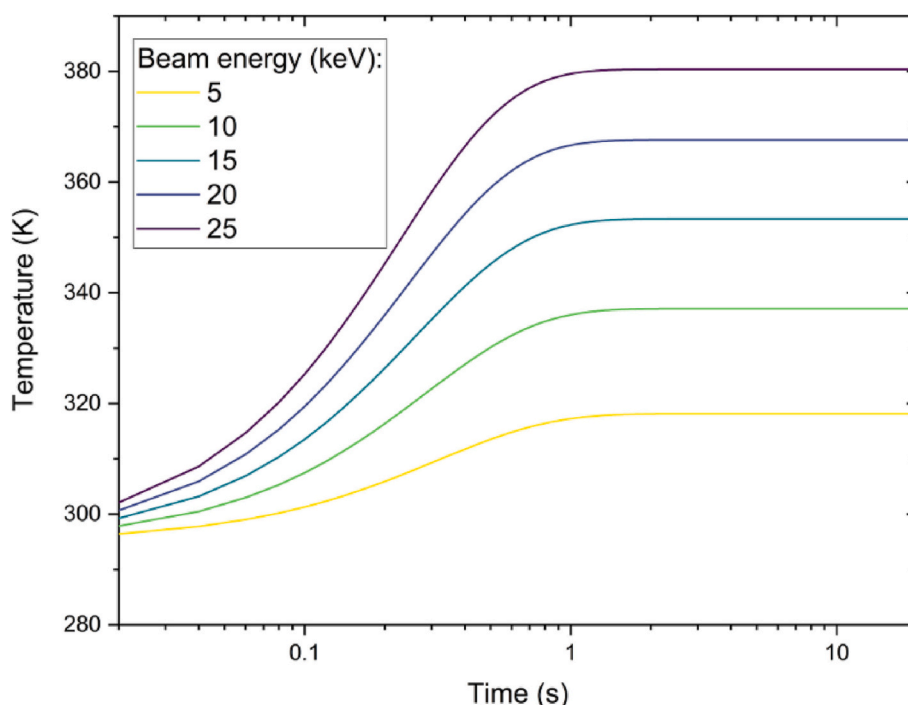


Fig. 9. Estimation of the temperature of collagen sample during implantation at different ion energies at a current density of $5 \mu\text{A cm}^{-2}$.

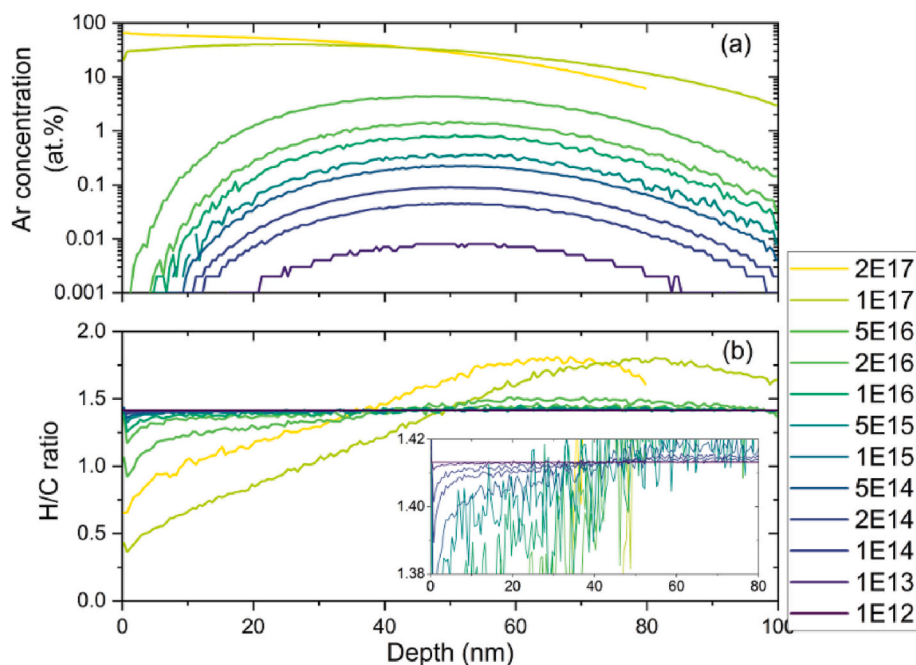


Fig. 10. Evolution of the implantation depth profile of Ar⁺ ion implantation (a) at 15 keV for the different implantation fluences and (b) at various energies and a fluence of $5 \times 10^{15} \text{ cm}^{-2}$.

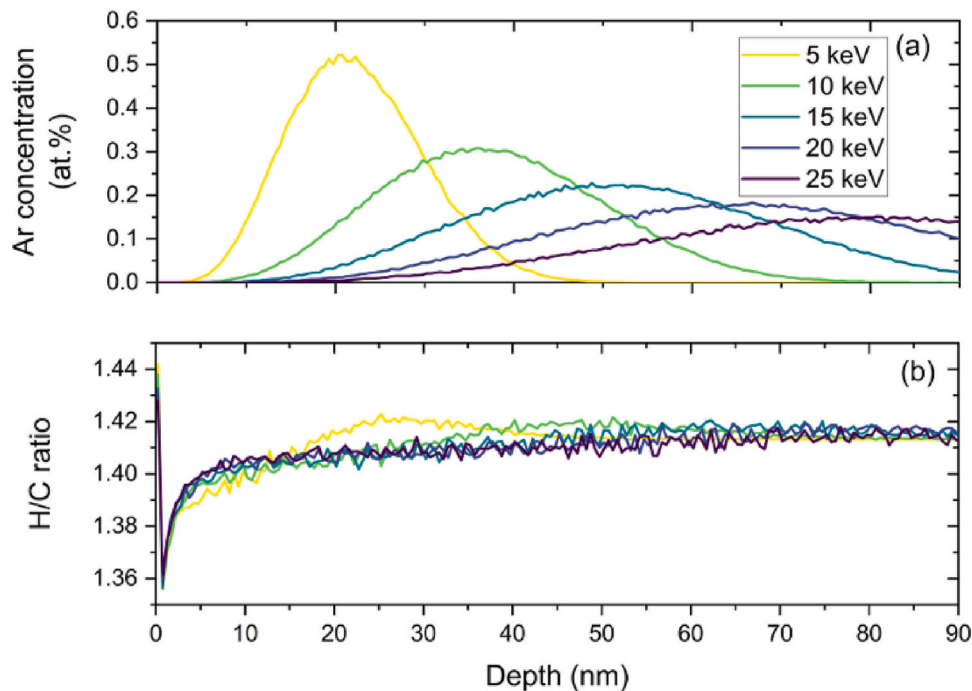


Fig. 11. (a) Ar concentration profile for implantation energy at $5 \times 10^{15} \text{ cm}^{-2}$ implantation fluence and (b) at various energies and a fluence of $5 \times 10^{15} \text{ cm}^{-2}$.

(Fig. 10(a)) and a simultaneous change in the H/C (Fig. 10(b)) ratio in collagen molecules. The changes in the H/C ratio in collagen can be attributed to the cascaded collisions within the sheet. Hydrogen is preferentially forward recoiled whereas the probability of backscattering is higher for carbon. This yields a depletion of hydrogen on the surface forming dehydrogenated amorphous carbon, while in the depth hydrogen is accumulated and a preferential formation of hydrogenated carbon occurs. This dehydrogenation mechanism explains the carbonisation (i.e., $\text{sp}^3 \text{ C-H}$ to $\text{sp}^2 \text{ C=C}$) on the surface of collagen observed in the Raman spectra.

At a fixed fluence of $5 \times 10^{15} \text{ cm}^{-2}$, variations in energies (ranging from 5 to 25 keV) affect the Ar implantation range, giving narrower distribution closer to the surface at lower energy (Fig. 11a). However, subtle differences were found in the H/C ratios at all energies (Fig. 11b). The small H/C ratio changes from 1.41 (unmodified) to 1.36 on the surface of collagen are consistent for all energies which supports the small minor influence of the acceleration energy observed in the spectra. This, again suggests the need of performing simulation alongside spectroscopic measurements for a more comprehensive understanding of the interactions of ion beam with materials.

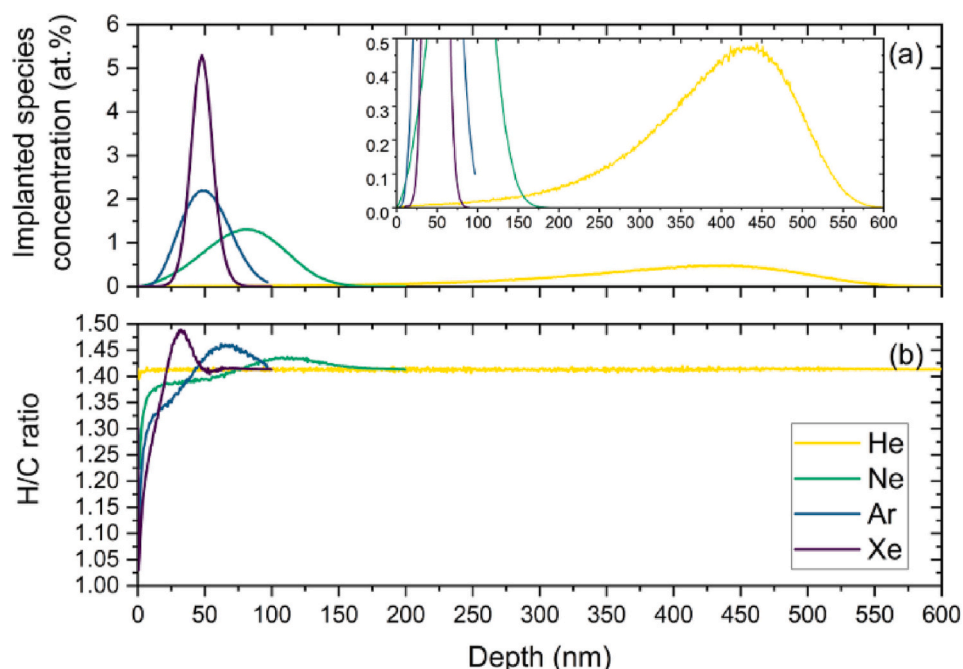


Fig. 12. Evolution of (a) the implantation depth profile and (b) the relative distribution of hydrogen for different implanted species 15 keV and a fluence of $5 \times 10^{15} \text{ cm}^{-2}$.

(Element) At the highest investigated fluence ($5E15$) at an energy of 15 keV, Raman spectroscopy revealed the dehydrogenation of aliphatic groups and the formation of C=C bonds in carbonaceous species. Ballistic transport simulations directly explain this effect. A heavier element has a higher nuclear stopping power (Fig. 8) which causes a narrower distribution of the noble gas closer to the surface (Fig. 12a). Simultaneously, the ballistic transport during ion implantation yields a hydrogen-depleted region near the surface and a hydrogen-rich region in the depth with transition points of 30 nm for Xe and 70 nm for Ar, respectively. Hence, the transition to heavier noble gases for implantation makes modifications more surface sensitive but also enhances amorphous carbon formation as observed by spectroscopic results.

4. Conclusions

While these results can be used directly to target specific concentrations of graphitic and hydrogenated amorphous carbon species at the surface of collagen, implantation of reactive species could further increase the range of functionalisation achievable with ion implantation. For example, we anticipate that oxygen, nitrogen, and fluorocarbon implantation could lead to different oxide, nitride, and fluoride species that could be used to target specific reactions on the surface. When investigating these implantations, it will be important to understand the contribution of ion beam damage to changes in chemistry from the implanted species. In that regard, the results presented here will guide the selection of ion beam parameters to appropriately functionalise collagen surfaces for a wide range of emerging biomedical and bio-electronic applications.

CRedit authorship contribution statement

Jérôme Leveueur: Writing – original draft, Resources, Conceptualization, Methodology, Resources, Validation, Formal analysis, Investigation, Visualization. **Yi Zhang:** Writing – original draft, Methodology, Formal analysis, Investigation, Visualization. **Holger Fiedler:** Writing – review & editing, Validation, Formal analysis, Investigation. **Sujay Prabakar:** Writing – review & editing, Supervision, Project administration, Funding acquisition, Resources. **Eric C. Le Ru:** Writing – review

& editing, Supervision, Resources, Validation. **John Kennedy:** Writing – review & editing, Project administration, Funding acquisition, Resources.

Declaration of competing interest

The authors declare that they have no known competing financial interests or personal relationships that could have appeared to influence the work reported in this paper.

Data availability

Data will be made available on request.

Acknowledgements

This work was funded by the Science for Technological Innovation National Science Challenge (SfTI) – Kia Kotahi Mai: Te Ao Pūtaiao me Te Ao Hangarau; and in part by the New Zealand Ministry for Business, Innovation and Employment (MBIE) SSIF fund under contract LSRX-1801, and GNS Science's SSIF funded project on *Materials for a Low Carbon Future* (C05X1702).

References

- [1] M. Meyer, Processing of collagen based biomaterials and the resulting materials properties, *Biomed. Eng. Online* 18 (1) (2019) 24, <https://doi.org/10.1186/s12938-019-0647-0>.
- [2] J.A.M. Ramshaw, Biomedical applications of collagens, *J. Biomed. Mater. Res. - B Appl. Biomater.* 104 (4) (2016) 665–675, <https://doi.org/10.1002/jbm.b.33541>.
- [3] A. Sionkowska, S. Skrzyński, K. Śmiechowski, A. Kołodziejczak, The review of versatile application of collagen, *Polym. Adv. Technol.* 28 (1) (2017) 4–9, <https://doi.org/10.1002/pat.3842>.
- [4] W. Peng, D. Li, K. Dai, Y. Wang, P. Song, H. Li, P. Tang, Z. Zhang, Z. Li, Y. Zhou, C. Zhou, Recent progress of collagen, chitosan, alginate and other hydrogels in skin repair and wound dressing applications, *Int. J. Biol. Macromol.* 208 (2022) 400–408, <https://doi.org/10.1016/j.ijbiomac.2022.03.002>.
- [5] Q. Luo, M.A. Hossen, Y. Zeng, J. Dai, S. Li, W. Qin, Y. Liu, Gelatin-based composite films and their application in food packaging: a review, *J. Food Eng.* (2022) 313, <https://doi.org/10.1016/j.jfoodeng.2021.110762>.
- [6] C.H. Lee, A. Singla, Y. Lee, Biomedical applications of collagen, *Int. J. Pharm.* 221 (1) (2001) 1–22, [https://doi.org/10.1016/S0378-5173\(01\)00691-3](https://doi.org/10.1016/S0378-5173(01)00691-3).

- [7] H.-J. Lee, S.-H. Ahn, G.H. Kim, Three-dimensional collagen/alginate hybrid scaffolds functionalized with a drug delivery system (DDS) for bone tissue regeneration, *Chem. Mater.* 24 (5) (2012) 881–891, <https://doi.org/10.1021/cm200733s>.
- [8] T.-Y. Wang, L.L. Kendrick-Williams, M.Y. Choy, K.A. Gilmore, T. Bonnard, H. A. Pearce, L.S. Law, I. Carmichael, S.H. Cody, K. Alt, Collagen-targeted theranostic nanospheres for delivery of the matrix metalloproteinase 14 inhibitor naphthofluorescein, *Chem. Mater.* 32 (9) (2020) 3707–3714, <https://doi.org/10.1021/acs.chemmater.9b02840>.
- [9] J. Gómez-Estaca, R. Gavara, R. Catalá, P. Hernández-Muñoz, The potential of proteins for producing food packaging materials: a review, *Packag. Technol. Sci.* 29 (4–5) (2016) 203–224, <https://doi.org/10.1002/pts.2198>.
- [10] N. Nassif, F. Gobeaux, J. Seto, E. Belamie, P. Davidson, P. Panine, G. Mosser, P. Fratzl, M.-M. Giraud Guille, Self-assembled collagen–apatite matrix with bone-like hierarchy, *Chem. Mater.* 22 (11) (2010) 3307–3309, <https://doi.org/10.1021/cm903594n>.
- [11] E.J. Bealer, K. Kavetsky, S. Dutko, S. Lofland, X. Hu, Protein and polysaccharide-based magnetic composite materials for medical applications, *Int. J. Mol. Sci.* 21 (1) (2019) 186, <https://doi.org/10.3390/ijms21010186>.
- [12] N. Raies-Hosseini, Y. Park, J.S. Lee, Flexible artificial synaptic devices based on collagen from fish protein with spike-timing-dependent plasticity, *Adv. Funct. Mater.* 28 (31) (2018) 1800553, <https://doi.org/10.1002/adfm.201800553>.
- [13] J.-S. Benas, L. Veeramuthu, Y.-Y. Chuang, S.-Y. Chuang, F.-C. Liang, C.-J. Cho, W.-Y. Lee, Y. Yan, Y. Zhou, C.-C. Kuo, Eco-friendly collagen-based bio-organic field effect transistor with improved memory characteristics, *Org. Electron.* 86 (2020), 105925, <https://doi.org/10.1016/j.orgel.2020.105925>.
- [14] L. Cen, W. Liu, L. Cui, W. Zhang, Y. Cao, Collagen tissue engineering: development of novel biomaterials and applications, *Pediatr. Res.* 63 (5) (2008) 492–496, <https://doi.org/10.1203/PDR.0b013e31816c5bc3>.
- [15] Y. Zeng, B. Sun, H.Y. Yu, X. Wang, H. Peng, Y. Chen, S. Zhu, S. Mao, W. Hou, A sustainable biomimetic memory device based on natural collagen, *Mater. Today Chem.* 13 (2019) 18–24, <https://doi.org/10.1016/j.mtchem.2019.04.008>.
- [16] H. Amani, H. Arzaghi, M. Bayandori, A.S. Dezfili, H. Pazoki-Toroudi, A. Shafiee, L. Moradi, Controlling cell behavior through the design of biomaterial surfaces: a focus on surface modification techniques, *Adv. Mater. Interfaces* 6 (13) (2019) 1–30, <https://doi.org/10.1002/admi.201900572>.
- [17] K. Lewandowska, A. Sionkowska, S. Grabka, B. Kaczmarek, Surface and thermal properties of collagen/hyaluronic acid blends containing chitosan, *Int. J. Biol. Macromol.* 92 (2016) 371–376, <https://doi.org/10.1016/j.ijbiomac.2016.07.055>.
- [18] A. Sionkowska, A. Planecka, J. Kozłowska, J. Skopińska-Wisniewska, Surface properties of UV-irradiated poly (vinyl alcohol) films containing small amount of collagen, *Appl. Surf. Sci.* 255 (7) (2009) 4135–4139, <https://doi.org/10.1016/j.apsusc.2008.10.108>.
- [19] T.G. Kim, H. Shin, D.W. Lim, Biomimetic scaffolds for tissue engineering, *Adv. Funct. Mater.* 22 (12) (2012) 2446–2468, <https://doi.org/10.1002/adfm.201103083>.
- [20] Y. Suzuki, Ion beam modification of polymers for the application of medical devices, *Nucl. Instrum. Methods Phys. Res., Sect. B* 206 (2003) 501–506, [https://doi.org/10.1016/S0168-583X\(03\)00808-5](https://doi.org/10.1016/S0168-583X(03)00808-5).
- [21] K. Adamiak, A. Sionkowska, The influence of UV irradiation on fish skin collagen films in the presence of xanthohumol and propanediol, *Spectrochim. Acta A Mol. Biomol. Spectrosc.* (2022) 282, <https://doi.org/10.1016/j.saa.2022.121652>.
- [22] K. Lau, C. Heu, M.J. Moore, A. Zhang, B. Akhavan, S.G. Wise, M.M.M. Bilek, M. S. Lord, J. Rnjak-Kovacina, Effect of plasma ion immersion implantation on physicochemical and biological properties of silk towards creating a versatile biomaterial platform, *Mater. Today Adv.* (2022) 13, <https://doi.org/10.1016/j.mtadv.2022.100212>.
- [23] R. Shah, B. Gashi, S. Hoque, M. Marian, A. Rosenkranz, Enhancing mechanical and biomedical properties of prostheses - surface and material design, *Surf. Interfaces* (2021) 27, <https://doi.org/10.1016/j.surfin.2021.101498>.
- [24] J.F. Ziegler, *Ion Implantation Science and Technology*, Elsevier, 2012.
- [25] F. Frost, R. Fechner, D. Flamm, B. Ziberi, W. Frank, A. Schindler, Ion beam assisted smoothing of optical surfaces, *Appl. Phys. A* 78 (5) (2004) 651–654, <https://doi.org/10.1007/s00339-003-2274-6>.
- [26] J. Muñoz-García, M. Castro, R. Cuerno, Nonlinear ripple dynamics on amorphous surfaces patterned by ion beam sputtering, *Phys. Rev. Lett.* 96 (8) (2006), 086101, <https://doi.org/10.1103/PhysRevLett.96.086101>.
- [27] M.A. Nastasi, J.W. Mayer, *Ion Implantation and Synthesis of Materials Vol. 80*, Springer, 2006.
- [28] T. Kamiya, S. Aiba, M. Miyakawa, K. Nomura, S. Matsuishi, K. Hayashi, K. Ueda, M. Hirano, H. Hosono, Field-induced current modulation in nanoporous semiconductor, electron-doped $12\text{CaO} \cdot 7\text{Al}_2\text{O}_3$, *Chem. Mater.* 17 (25) (2005) 6311–6316, <https://doi.org/10.1021/cm051904s>.
- [29] B.L. Doyle, F.D. McDaniel, R.W. Hamm, The future of industrial accelerators and applications, *Rev. Accel. Sci. Technol.* 10 (01) (2019) 93–116, <https://doi.org/10.1142/S1793626819300068>.
- [30] Ionics, *SMART surfaces*. 28 September 2021]; Available from: <https://www.ionics-group.com/en>.
- [31] *Walibeam*. 28 September 2021]; Available from: <http://www.walibeam.com/>.
- [32] W.K. Choi, S.K. Koh, H.J. Jung, Surface chemical reaction between polycarbonate and kilo-electron-volt energy Ar^+ ion in oxygen environment, *J. Vac. Sci. Technol. A* 14 (4) (1996) 2366–2371, <https://doi.org/10.1116/1.580024>.
- [33] E.H. Lee, Ion-beam modification of polymeric materials—fundamental principles and applications, *Nucl. Instrum. Methods Phys. Res., Sect. B* 151 (1–4) (1999) 29–41, [https://doi.org/10.1016/S0168-583X\(99\)00129-9](https://doi.org/10.1016/S0168-583X(99)00129-9).
- [34] H. Dong, T. Bell, State-of-the-art overview: ion beam surface modification of polymers towards improving tribological properties, *Surf. Coat. Technol.* 111 (1) (1999) 29–40, [https://doi.org/10.1016/S0257-8972\(98\)00698-7](https://doi.org/10.1016/S0257-8972(98)00698-7).
- [35] A. Kondyurin, M. Bilek, *Ion Beam Treatment of Polymers: Application Aspects from Medicine to Space*, Newnes, 2014.
- [36] A. Chapiro, *Radiation chemistry of polymers*, *Radiat. Res. Suppl.* 4 (1964) 179–191.
- [37] S.B. Wahed, C.R. Dunstan, P.A. Boughton, A.J. Ruys, S.N. Faisal, T.B. Wahed, B. Salahuddin, X. Cheng, Y. Zhou, C.H. Wang, M.S. Islam, S. Aziz, Functional ultra-high molecular weight polyethylene composites for ligament reconstructions and their targeted applications in the restoration of the anterior cruciate ligament, *Polymers* 14 (11) (2022), <https://doi.org/10.3390/polym14112189>.
- [38] Y. Chen, C. Xu, C.H. Wang, M.M.M. Bilek, X. Cheng, An effective method to optimise plasma immersion ion implantation: sensitivity analysis and design based on low-density polyethylene, *Plasma Process. Polym.* 19 (6) (2022), <https://doi.org/10.1002/ppap.202100199>.
- [39] K. Kurotobi, M. Kaibara, Y. Suzuki, M. Iwaki, H. Nakajima, S. Kaneko, Ion implantation into collagen-coated surfaces for the development of small diameter artificial grafts, *Colloids Surf. B: Biointerfaces* 19 (3) (2000) 227–235, [https://doi.org/10.1016/S0927-7765\(00\)00160-0](https://doi.org/10.1016/S0927-7765(00)00160-0).
- [40] D. Li, W. Yang, G.Y. Li, Extraction of native collagen from limed bovine split wastes through improved pretreatment methods, *J. Chem. Technol. Biotechnol.* 83 (7) (2008) 1041–1048, <https://doi.org/10.1002/jctb.1912>.
- [41] H.W. Ng, Y. Zhang, R. Naffa, S. Prabakar, Monitoring the degradation of collagen hydrogels by collagenase clostridium histolyticum, *Gels* 6 (4) (2020) 46, <https://doi.org/10.3390/gels6040046>.
- [42] A. Markwitz, J. Kennedy, Group-IV and V ion implantation into nanomaterials and elemental analysis on the nanometre scale, *Int. J. Nanotechnol.* 6 (3–4) (2009) 369–383, <https://doi.org/10.1504/IJNT.2009.022926>.
- [43] H. Fiedler, P. Gupta, J. Kennedy, A. Markwitz, 28 Si⁺ ion beams from Penning ion source based implanter systems for near-surface isotopic purification of silicon, *Rev. Sci. Instrum.* 89 (12) (2018), <https://doi.org/10.1063/1.5048949>.
- [44] A. Mutzke, R. Schneider, S. Eckstein, R. Dohmen, *SDTrimSP Version 5.0 IPP Report 12/8*, Max-Planck-Institut für Plasmaphysik, 2011.
- [45] J. Leveneur, A. Rajan, J. McDonald-Wharry, M.-J. Le Guen, K. Pickering, J. Kennedy, Structural and chemical changes of cellulose fibres under low energy ion implantations, *Surf. Coat. Technol.* 355 (2018) 191–199, <https://doi.org/10.1016/j.surfcoat.2018.04.006>.
- [46] A. Bhattacharya, R. Mahajan, Temperature dependence of thermal conductivity of biological tissues, *Physiol. Meas.* 24 (3) (2003) 769, <https://doi.org/10.1088/0967-3334/24/3/312>.
- [47] M. Pyda, P. Zawada, A. Drogon, M. Skotnicki, P. Cebe, Vibrational heat capacity of collagen and collagen–water, *J. Therm. Anal. Calorim.* 138 (5) (2019) 3389–3401, <https://doi.org/10.1007/s10973-019-08697-5>.
- [48] B.G. Frushour, J.L. Koenig, Raman scattering of collagen, gelatin, and elastin, *Biopolymers* 14 (2) (1975) 379–391, <https://doi.org/10.1002/bip.1975.360140211>.
- [49] C. Gullekson, L. Lucas, K. Hewitt, L. Kreplak, Surface-sensitive Raman spectroscopy of collagen I fibrils, *Biophys. J.* 100 (7) (2011) 1837–1845, <https://doi.org/10.1016/j.bpj.2011.02.026>.
- [50] S. Stewart, P.M. Fredericks, Surface-enhanced Raman spectroscopy of peptides and proteins adsorbed on an electrochemically prepared silver surface, *Spectrochim. Acta A Mol. Biomol. Spectrosc.* 55 (7–8) (1999) 1615–1640, [https://doi.org/10.1016/S1386-1425\(98\)00293-5](https://doi.org/10.1016/S1386-1425(98)00293-5).
- [51] K.A. Dehring, A.R. Smukler, B.J. Roessler, M.D. Morris, Correlating changes in collagen secondary structure with aging and defective type II collagen by Raman spectroscopy, *Appl. Spectrosc.* 60 (4) (2006) 366–372, <https://doi.org/10.1366/000370206776593582>.
- [52] A. Rygula, K. Majzner, K.M. Marzec, A. Kaczor, M. Pilarczyk, M. Baranska, Raman spectroscopy of proteins: a review, *J. Raman Spectrosc.* 44 (8) (2013) 1061–1076, <https://doi.org/10.1002/jrs.4335>.
- [53] M. Unal, H. Jung, O. Akkus, Novel Raman spectroscopic biomarkers indicate that postyield damage denatures bone’s collagen, *J. Bone Miner. Res.* 31 (5) (2016) 1015–1025, <https://doi.org/10.1002/jbmr.2768>.
- [54] Y. Zhang, S. Prabakar, E.C. Le Ru, Coadsorbed species with halide ligands on silver nanoparticles with different binding affinities, *J. Phys. Chem. C* 126 (20) (2022) 8692–8702, <https://doi.org/10.1021/acs.jpcc.2c01092>.
- [55] M. Jastrzebska, R. Wrzalik, A. Kocot, J. Zalewska-Rejda, B. Cwalina, Raman spectroscopic study of glutaraldehyde-stabilized collagen and pericardium tissue, *J. Biomater. Sci. Polym. Ed.* 14 (2) (2003) 185–197, <https://doi.org/10.1163/156856203321142605>.
- [56] A.C. Ferrari, J. Robertson, Interpretation of Raman spectra of disordered and amorphous carbon, *Phys. Rev. B* 61 (20) (2000) 14095, <https://doi.org/10.1103/PhysRevB.61.14095>.
- [57] J.-B. Wu, M.-L. Lin, X. Cong, H.-N. Liu, P.-H. Tan, Raman spectroscopy of graphene-based materials and its applications in related devices, *Chem. Soc. Rev.* 47 (5) (2018) 1822–1873, <https://doi.org/10.1039/C6CS00915H>.
- [58] Y. Zhang, M. Mehta, B.W. Mansel, H.W. Ng, Y. Liu, G. Holmes, E.C. Le Ru, S. Prabakar, Anion-regulated binding selectivity of Cr(III) in collagen, *Biopolymers* (2020), e23406, <https://doi.org/10.1002/bip.23406>.
- [59] J.J. Cárcamo, A.E. Aliaga, E. Clavijo, C. Garrido, J.S. Gómez-Jeria, M.M. Campos-Valette, Proline and hydroxyproline deposited on silver nanoparticles. A Raman, SERS and theoretical study, *J. Raman Spectrosc.* 43 (6) (2012) 750–755, <https://doi.org/10.1002/jrs.3092>.

- [60] S.K. Kim, M.S. Kim, S.W. Suh, Surface-enhanced Raman scattering (SERS) of aromatic amino acids and their glycyI dipeptides in silver sol, *J. Raman Spectrosc.* 18 (3) (1987) 171–175, <https://doi.org/10.1002/jrs.1250180305>.
- [61] H. Shurvell, F. Bergin, Raman spectra of L (+)-glutamic acid and related compounds, *J. Raman Spectrosc.* 20 (3) (1989) 163–168, <https://doi.org/10.1002/jrs.1250200307>.
- [62] Z. Movasaghi, S. Rehman, I.U. Rehman, Raman spectroscopy of biological tissues, *Appl. Spectrosc. Rev.* 42 (5) (2007) 493–541, <https://doi.org/10.1080/05704920701551530>.
- [63] E.B. Wilson Jr., The normal modes and frequencies of vibration of the regular plane hexagon model of the benzene molecule, *Phys. Rev.* 45 (10) (1934) 706, <https://doi.org/10.1103/PhysRev.45.706>.
- [64] H. Ye, U. Rahul, T. Kruger, S. Wang, J. Norfleet Shi, S. De, Burn-related collagen conformational changes in ex vivo porcine skin using Raman spectroscopy, *Sci. Rep.* 9 (1) (2019) 1–9, <https://doi.org/10.1038/s41598-019-55012-1>.
- [65] M. Janko, P. Davydovskaya, M. Bauer, A. Zink, R.W. Stark, Anisotropic Raman scattering in collagen bundles, *Opt. Lett.* 35 (16) (2010) 2765–2767, <https://doi.org/10.1364/OL.35.002765>.
- [66] A. Masic, L. Bertinetti, R. Schuetz, L. Galvis, N. Timofeeva, J.W. Dunlop, J. Seto, M. A. Hartmann, P. Fratzl, Observations of multiscale, stress-induced changes of collagen orientation in tendon by polarized Raman spectroscopy, *Biomacromolecules* 12 (11) (2011) 3989–3996, <https://doi.org/10.1021/bm201008b>.
- [67] L. Van Gulick, C. Saby, H. Morjani, A. Beljebbar, Age-related changes in molecular organization of type I collagen in tendon as probed by polarized SHG and Raman microspectroscopy, *Sci. Rep.* 9 (1) (2019) 1–12, <https://doi.org/10.1038/s41598-019-43636-2>.
- [68] T. Riaz, R. Zeeshan, F. Zarif, K. Ilyas, N. Muhammad, S.Z. Safi, A. Rahim, S.A. Rizvi, I.U. Rehman, FTIR analysis of natural and synthetic collagen, *Appl. Spectrosc. Rev.* 53 (9) (2018) 703–746, <https://doi.org/10.1080/05704928.2018.1426595>.
- [69] K. Belbachir, R. Noreen, G. Gouspillou, C. Petibois, Collagen types analysis and differentiation by FTIR spectroscopy, *Anal. Bioanal. Chem.* 395 (3) (2009) 829–837, <https://doi.org/10.1007/s00216-009-3019-y>.
- [70] M. Jackson, P.H. Watson, W.C. Halliday, H.H. Mantsch, Beware of connective tissue proteins: assignment and implications of collagen absorptions in infrared spectra of human tissues, *Biochim. Biophys. Acta - Mol. Basis Dis.* 1270 (1) (1995) 1–6, [https://doi.org/10.1016/0925-4439\(94\)00056-V](https://doi.org/10.1016/0925-4439(94)00056-V).
- [71] A. Sionkowska, Effects of solar radiation on collagen and chitosan films, *J. Photochem. Photobiol. B Biol.* 82 (1) (2006) 9–15, <https://doi.org/10.1016/j.jphotobiol.2005.08.003>.
- [72] L. Rieppo, S. Saarakkala, T. Närhi, H. Helminen, J. Jurvelin, J. Rieppo, Application of second derivative spectroscopy for increasing molecular specificity of fourier transform infrared spectroscopic imaging of articular cartilage, *Osteoarthritis Cartil.* 20 (5) (2012) 451–459, <https://doi.org/10.1016/j.joca.2012.01.010>.
- [73] W. Hübner, A. Blume, R. Pushnjakova, Y. Dekhtyar, H.-J. Hein, The influence of X-ray radiation on the mineral/organic matrix interaction of bone tissue: an FT-IR microscopic investigation, *Int. J. Artif. Organs* 28 (1) (2005) 66–73, <https://doi.org/10.1177/039139880502800111>.